Key vortical structure causing laminar-turbulent transition in a boundary layer disturbed by a short-duration jet

Joe Yoshikawa, Yu Nishio, Seiichiro Izawa, and Yu Fukunishi
Department of Mechanical Systems and Design, Graduate School of Engineering, Tohoku University, 6-6-01, Aramaki-Aoba, Aoba-ku, Sendai 980-8579, Japan

(Received 1 July 2017; published 23 January 2018)

Numerical simulations are carried out to discover the flow structure that plays an important role in the laminar-turbulent transition process of a boundary layer on a flat plate. The boundary layer is destabilized by ejecting a short-duration jet from a hole in the surface. When the jet velocity is set to 20% of the uniform-flow velocity, a laminar-turbulent transition takes place, whereas in the 18% case, the disturbances created by the jet decay downstream. It is found that in both cases, hairpin vortices are generated; however, these *first-generation* hairpins do not directly cause the transition. Only in the 20% case does a new hairpin vortex of a different shape with wider distance between the legs appear. The new hairpin grows with time and evokes the generation of vortical structures one after another around it, turning the flow turbulent. It is found that the difference between the two cases is whether or not one of the first-generation hairpin vortices gets connected with the nearby longitudinal vortices. Only when the connection is successful is the new hairpin vortex with wider distance between the legs created. For each of several cases tested with changing jet-ejecting conditions, no difference is found in the importance of the role of the hairpin structure. Therefore, we conclude that the hairpin vortex with widespread legs is a key structure in the transition to turbulence.

DOI: 10.1103/PhysRevFluids.3.013904

I. INTRODUCTION

The transition of a boundary layer from a laminar state to a turbulent state is a fundamental engineering issue that has been studied. The transition process and the formation of a predominant structure depend on the freestream turbulence level. In a low-disturbance environment, linear two-dimensional perturbations, or Tollmien-Schlichting waves (T-S waves), start to grow in a laminar boundary layer. Accompanying the three-dimensionalization of T-S waves, Λ vortices are generated, whose breakdowns trigger the generation of isolated turbulent regions [1]. In contrast, in a high-disturbance environment, a bypass transition takes place, wherein a streaky structure is generated, followed by the quasistreamwise vortices or hairpin vortices that queue up in the streamwise direction to eventually break down. The secondary instability of streaky structures is responsible for the formation of these vortices [2]. Asai *et al.* [3] discussed the transient growth and the eventual breakdown of a low-speed streak, which was artificially generated by sucking out the near-wall turbulent structures from a fully developed turbulent boundary layer.

Other transition processes triggered by the growth of localized disturbances in a Blasius boundary layer have also been studied. Based on their theoretical analysis and experiments, Gaster [4] and Gaster *et al.* [5], followed the development of wave packets introduced inside a flat-plate boundary layer. Asai *et al.* [6] examined the subcritical transition triggered by energetic hairpin vortices, which were acoustically excited at the leading edge. They found that the transition was likely to occur at subcritical Reynolds numbers when the x-Reynolds number was over $\mathrm{Re}_x = 3.9 \times 10^4$. A similar study was performed by Lemoult *et al.* [7] in a plane Poiseuille flow. They found that

the minimal amplitude of the perturbation triggering the transition could be asymptotically scaled by the inverse of the Reynolds number, Re^{-1}, in the range of $\mathrm{Re} > 2000$. In addition, Levin and Henningson [8] found hairpin vortices and spiral vortices accompanying the generation of a turbulent spot inside an asymptotic suction boundary layer. Singer and Joslin [9] pointed out that when a short-duration jet was ejected from a slit in a flat plate, the structures would appear in the following order: a first hairpin vortex, a second hairpin vortex, quasistreamwise vortices, and a turbulent spot. Cherubini *et al.* [10,11] obtained optimal perturbations by controlling the energies of the disturbances introduced into the boundary layer under both linear and nonlinear conditions. They found that the "streak-dominated" and the "hairpin-dominated" structure were optimal perturbations in the linear and nonlinear condition, respectively.

Hairpin-shaped vortical structures have been widely observed in turbulent spots, turbulent boundary layers, and turbulent pipe and channel flow. Singer [12] discovered many streamwise vortices and hairpin vortices inside a turbulent spot, with streamwise vortices near the interface, which played a vital role in pulling the surrounding fluid in the laminar region to the turbulent spot. Farano *et al.* [13] looked for the nonlinear optimal perturbation in a plane Poiseuille flow, as well as Cherubini *et al.* [10,11], and obtained three vortex pairs that were inclined in the streamwise direction and symmetric in the spanwise direction. They observed that the initial optimal perturbation grew quickly and nonlinearly into a hairpin-shaped vortical structure that created turbulence, and concluded that the nonlinear growing process of these hairpin vortices was the reason behind observing the hairpins frequently. Acarlar and Smith [14] performed a visualization experiment by continuously ejecting a jet of dyed solution from the slit of a flat plate placed inside a water channel and observed the process wherein the head of a new hairpin vortex was formed between the legs of the preceding hairpin. Stoke *et al.* [15] simulated similar flow fields of laminar and turbulent boundary layers and performed stability analyses of the velocity profiles immediately prior to the appearance of hairpin vortices. They found that hairpin vortices were caused by an inflectional point type instability regardless of the state of the boundary layer. The evolution of the packet of hairpin vortices has also been investigated for pipe flows (see, e.g., Philip and Cohen [16] and Mehta and Cohen [17]) and channel flows (see, e.g., Zhou *et al.* [18]).

Both transverse and crossflow jets have widely been used in flow control for boundary layers and separations. The stability and structural characteristics of transverse jets are well described in Bagheri *et al.* [19], Mahesh [20], and Karagozian [21]. In most of these applications, jets with jet-to-crossflow velocity ratios $v_{\mathrm{jet}}/U_\infty$ that are much higher than unity are used. However, to be used in a laminar boundary layer, the transverse jet of $v_{\mathrm{jet}}/U_\infty > 1$ may strongly disturb the flow field. For this reason, the strength of the short-duration jet Singer and Joslin [9] ejected was $v_{\mathrm{jet}}/U_\infty = 0.25$ and that of the continuously blowing jet Stoke *et al.* [15] used was $v_{\mathrm{jet}}/U_\infty = 0.2$. The strengths of the jets used in this research are also much smaller than unity.

Substantial knowledge on how vortical structures evolve during the transition process has been accumulated. However, in our opinion, our knowledge is not sufficient. For example, we still do not know the flow structure which plays the essential role in initiating the laminar-turbulent transition. Hence, the present study aims to identify the key structure that triggers such a transition. Two numerical results are prepared, changing only the velocity of the short-duration jet ejected from the wall into a Blasius boundary layer. In the first case, the flow field became turbulent downstream, whereas, in the second case, the flow field returned to the laminar state. The key structures and mechanisms that led to this significant difference downstream are discussed in this paper.

II. COMPUTATIONAL METHOD

The three-dimensional incompressible Navier-Stokes equations and the continuity equation are solved using a finite-difference method. To capture the growth of target velocity fluctuations with high accuracy, velocity and pressure fields are decomposed into base-flow and fluctuation components, and only the fluctuation components are computed. The Blasius boundary layer is given as the base flow. The marker and cell (MAC) method is adopted as a computational algorithm, and the

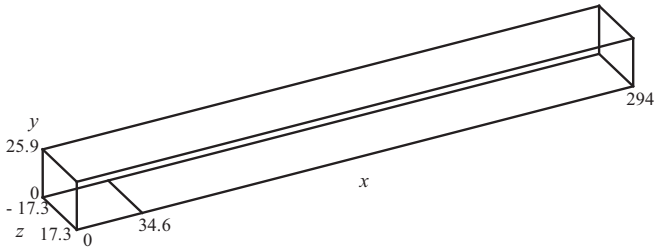

(a) Overall view

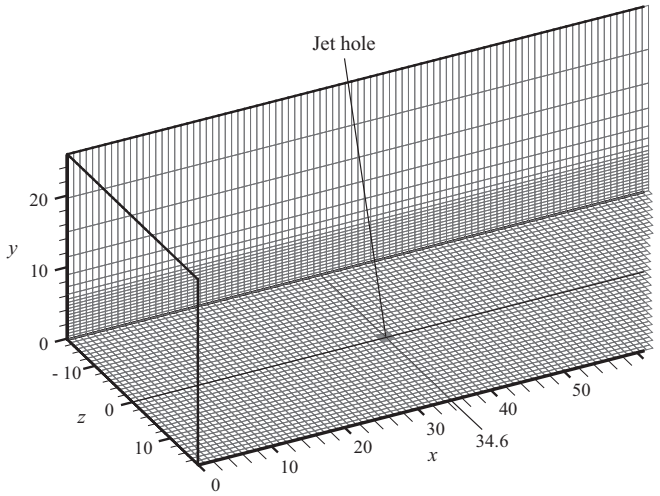

(b) Close-up view around the jet hole

FIG. 1. Computational domain.

second-order accurate Crank-Nicolson semi-implicit method is used for time integration. The second-order accurate central-difference scheme is applied to the spatial derivatives, except for the convection terms, which are discretized by the third-order upstream difference scheme (K-K scheme [22]). The successive over-relaxation (SOR) method with relaxation factor = 1.97 is used to solve the Poisson equation of pressure. When the velocity of the next time step is calculated, the spatial derivatives are computed by the multidirectional difference scheme [23], in which the derivatives of four different coordinate systems, the original and three others rotated by an angle of 45° around each axis, are added with the weighting 6:1:1:1. The computational code is parallelized by OpenMP.

Figure 1 shows a computational domain. The size of the rectangular computational domain is $294 \times 25.9 \times 34.6$. The origin of the coordinate system is located at the spanwise center and on the wall of the inlet boundary, where the x, y, and z axes denote the streamwise, wall-normal, and spanwise directions, respectively. The coordinates and the physical properties used in this paper are nondimensionalized by the uniform-flow velocity U_∞ and the displacement thickness of the Blasius boundary layer at the inlet boundary, δ_0^*. The grid points number is $1701 \times 101 \times 201$. The computational grid is equally spaced in the streamwise and spanwise directions. In the wall-normal direction, grid points are equally spaced only for the first 61 points from the plate surface, and the grid spacing gradually increases toward the outer boundary. The maximum height of the equally spaced grid is 5.18, which is larger than the thickness of the laminar boundary layer at the outlet boundary, 4.51. The rate of change in the grid intervals in the wall-normal direction is 1.1 at maximum. A time interval is 0.043, which corresponds to Courant number of 0.25. It should be noted that, for comparison, we also performed another simulation with higher resolution in which the grid numbers

TABLE I. Jet-ejecting parameters.

	Re_{δ^*}	v_{jet}	$l_x \times l_z$	T_{jet}	Transition
Reference (A)	663	0.18	1.73×1.73	13.0	No
Reference (B)	663	0.20	1.73×1.73	13.0	Yes
	456	0.30	1.73×1.73	13.0	No
	456	0.33	1.73×1.73	13.0	Yes
	867	0.12	1.73×1.73	13.0	No
	867	0.14	1.73×1.73	13.0	Yes
	663	0.25	1.73×1.04	13.0	No
	663	0.28	1.73×1.04	13.0	Yes
	663	0.16	1.73×2.76	13.0	No
	663	0.18	1.73×2.76	13.0	Yes
	663	0.18	1.73×1.73	19.0	Yes

were 1.2 times larger in each direction, and no intrinsic differences were found in the growth of vortical structures.

A short-duration jet is modeled by giving a uniform vertical velocity v_{jet} through the duration of T_{jet} at a small region of $l_x \times l_z$ in the plate surface, whose center is fixed at $x = 34.6$ and $z = 0$. The jet is ejected into a boundary layer starting at $t = 0$. A typical size of the jet region is $l_x = l_z = 1.73$, and the typical ejection duration of $T_{\mathrm{jet}} = 13.0$, which we call the reference cases. This ejection duration is shorter than the time needed for the first coherent structure induced by the jet to build itself in the boundary layer. The Reynolds number based on the local displacement thickness Re_{δ^*} is 613 at the inlet and 663 at the hole location. The jet location is inside the supercritical region, because the critical Re_{δ^*} given by the Orr-Sommerfeld stability equation is 520. In addition to the reference case, several different cases changing the ejection duration, the aspect ratio of ejection hole, and the ejection location are carried out for comparison. The computational conditions are summarized in Table I.

Because the difference from the Blasius boundary layer is treated as a velocity fluctuation, the velocity boundary conditions are set to zero at the inlet boundary and the wall surface, i.e., the steady-inflow condition and the nonslip condition, respectively. Also, the derivative values of the velocity fluctuations are set to zero at the outlet boundary and the far boundary. The derivatives of the pressure fluctuation are set to zero at the inlet, outlet, top, and wall boundaries. Periodic boundary conditions are applied in the spanwise direction for both the velocity and pressure fluctuations.

III. RESULTS AND DISCUSSION

The jet-ejecting velocities v_{jet} necessary to trigger the transition to turbulence take different values depending on the flow conditions, such as the Reynolds number, size of the jet hole, and duration of the jet. Simulations are performed under the conditions shown in Table I. It is known that, in general, the jet velocity necessary to trigger the turbulent transition decreases in proportion to $\mathrm{Re}_{\delta^*}^{\gamma}$. The value of exponent γ varies depending on the flow field. For example, $\gamma = -1.5$ for a parallel boundary layer such as an asymptotic suction boundary layer (Levin and Henningson [8]) and $\gamma = -1$ for a plane Poiseuille flow (Lemoult *et al.* [7]). The initial disturbances of the former direct numerical simulations [8] were given in the forms of two counter-rotating vortex pairs, while the continuous injection was used in the latter water channel experiment [7]. A similar tendency was reported by Peixinho and Mullin [24] for a pipe Poiseuille flow. Peixinho and Mullin found that the scaling exponent lies in the range of $-1.5 \leqslant \gamma \leqslant -1.3$ depending on the orientations of the push-pull disturbances, which were lower than those for the simple ejections for which $\gamma = -1$. The result of our study is shown in Fig. 2. In our case the critical velocity required to cause the transition to turbulence scales as $\mathrm{Re}_{\delta^*}^{-1.38}$ or expressed in a different notation, the Reynolds number based on

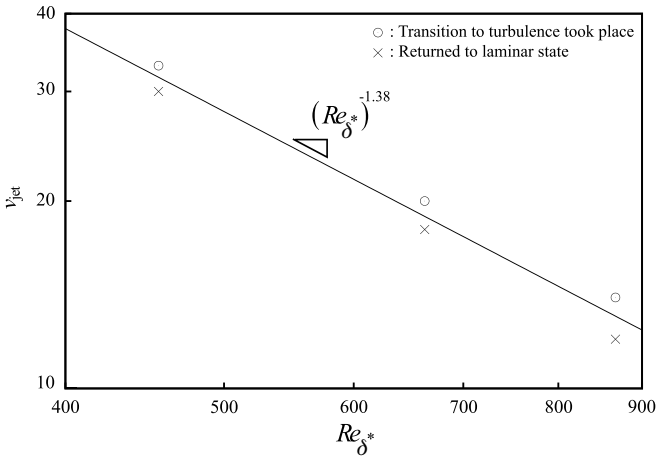

FIG. 2. Jet velocities needed to trigger the transition to turbulence under different Reynolds number conditions.

the discharge volume $\mathrm{Re}_j = (v_{\mathrm{jet}} l_x l_z)/(\nu l_z)$ scales as $l_z^{-0.488}$. This value is close to the $\gamma = -0.5$ exponent for a pipe Poiseuille flow, obtained by Peixinho and Mullin [24].

A. Comparison of two cases under different jet velocity v_{jet}

The time variations of vortex volumes for the reference cases are presented in Fig. 3. Throughout this paper, unless otherwise noted, a point that satisfies $Q \geqslant 0.002$ is regarded as being inside a vortex, where Q denotes the second invariant of a velocity-gradient tensor. Total vortex volume is measured by counting the number of grid points satisfying $Q \geqslant 0.002$. The jet is ejected from $t = 0$ through 13.0. In both the $v_{\mathrm{jet}} = 0.18$ [reference case (A)] and $v_{\mathrm{jet}} = 0.20$ [reference case (B)] jet-velocity cases, the vortex volumes first increase and then start to decrease around $t \gtrsim 100$. In the $v_{\mathrm{jet}} = 0.18$ case, the total volume continues to decrease with time and the flow field eventually

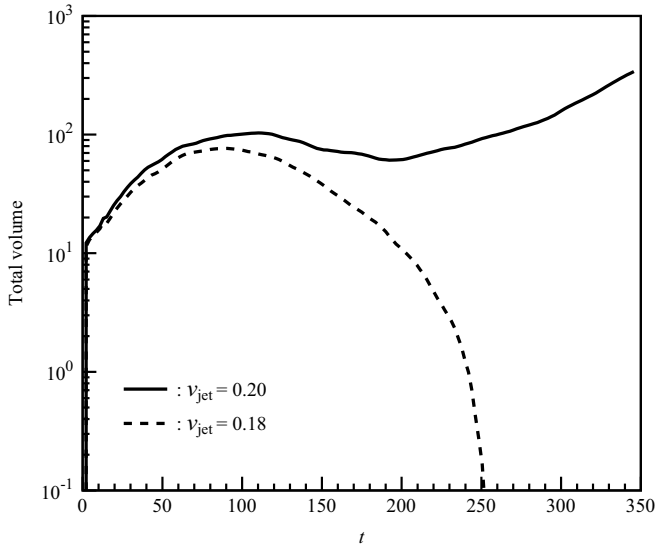

FIG. 3. Time variation of vortex volume defined as $Q \geqslant 0.002$.

returns to a laminar state. However, in the $v_{\text{jet}} = 0.20$ case, the vortex volume resumes increasing after $t \simeq 190$ and never decreases again.

The changes in the vortical structures are compared in Fig. 4. The surface of each structure is painted in colors depending on the local streamwise vorticity, ω_x. Here red and blue correspond to positive and negative streamwise vorticities, respectively. Black lines on the plate surface are drawn at a normalized interval of 10 in the streamwise direction and 5 in the spanwise direction. At $t = 34.6$, in both cases, two hairpin vortices with their heads upright are generated immediately downstream of the jet hole at $z = 0$. Hereafter, these hairpin vortices will be called the *first-generation* hairpins. In the figure, two more vortices are found around the hairpins. Vortex A appears on the downstream side, and vortex B appears on the upstream side, both near the wall. Vortex B resembles the so-called "necklace vortex," which is often observed at the bottom of bridge piers. As time passes, new hairpin vortices are generated one after another on the upstream side of the original hairpin. A similar phenomenon, whereby a hairpin vortex generates new ones in sequence, was observed in the water-channel experiments of Acarlar *et al.* [14] and Sabatino *et al.* [25]. Although no remarkable differences can be observed between the $v_{\text{jet}} = 0.18$ [reference case (A)] and $v_{\text{jet}} = 0.20$ [reference case (B)] cases up until $t = 103.7$, the differences become obvious after $t = 172.8$. In the weaker-jet ($v_{\text{jet}} = 0.18$) case, vortices A and B are temporarily elongated in the streamwise direction but soon disappear. Finally, no vortical structures survive in the flow field. On the other hand, in the stronger-jet case [reference case (B)], vortex A appears to be much stronger, and at $t = 207.4$, a new hairpin vortex appears on its upstream side.

Hereafter, we focus on the stronger-jet case [reference case (B)]. Figure 5 shows the time variation of vortical structures after $t = 172.8$ for the $v_{\text{jet}} = 0.20$ case [reference case (B)]. Thorns C found on the longitudinal vortex A at $t = 172.8$ are the remainders of the end of longitudinal vortex B above the legs of the vortex A as observed in Figs. 4(c) and 4(d). Two thorns C become connected to each other and form a spanwise vortex at $t = 190.1$. After $t = 190.1$, this spanwise vortex C reconnects with vortex pair A2, which are the upstream parts of vortex pair A, forming a new hairpin vortex, D, found in Fig. 5(c) at $t = 224.6$. At $t = 241.9$, spanwise vortex E newly appears between the legs of the hairpin vortex D and slightly away from the wall. Vortex E changes its shape into a V-shaped vortex at $t = 259.2$. The legs of the V-shaped vortex are tilted in the opposite direction compared with hairpin vortex D. The head part of the V-shaped vortex E located around $x = 170$ at $t = 259.2$ reconnects with the vortex pair D2, which constitute the upstream parts of the legs of the hairpin vortex D, and at $t = 276.5$ forms a new hairpin vortex, F. At $t = 289.4$, two thorns G appear in the middle of the legs of the hairpin vortex F, which merge into the V-shaped vortex G at $t = 311.0$. The process is similar to the mechanism by which spanwise vortex C was generated. At $t = 328.3$, the head part of vortex G reconnects with vortex pair F2 and forms a new hairpin vortex, H. After that, at $t = 345.6$, V-shaped vortex I appears above hairpin vortex H through the process already described above. In this way, hairpin vortices and V-shaped vortices are alternately generated. Through this process, the boundary layer becomes filled with many vortices, which become entangled with one another, eventually reaching a turbulent state at $t = 345.6$. Hereafter, the hairpin vortices generated after hairpin vortex D will be referred to as the *second-generation* hairpins.

B. First-generation and second-generation hairpin vortices

Let us compare the first-generation and second-generation hairpin vortices. Although the first-generation hairpin vortices are generated through a process of creation of a new head as a spanwise vortex connecting the legs of a preceding hairpin vortex, as was shown in Fig. 4, the hairpins of the second-generation are generated posterior to the creation of V-shaped vortices. The fundamental difference is that although the first-generation hairpins dissipate downstream without causing a transition, the second-generation hairpins produce complicated vortical structures one after another, resulting in a turbulent transition.

The details of the difference in such vortex regeneration processes are examined. Figure 6 shows the top and side views of the first-generation hairpins at $t = 103.7$. In the side view (b) of the figure,

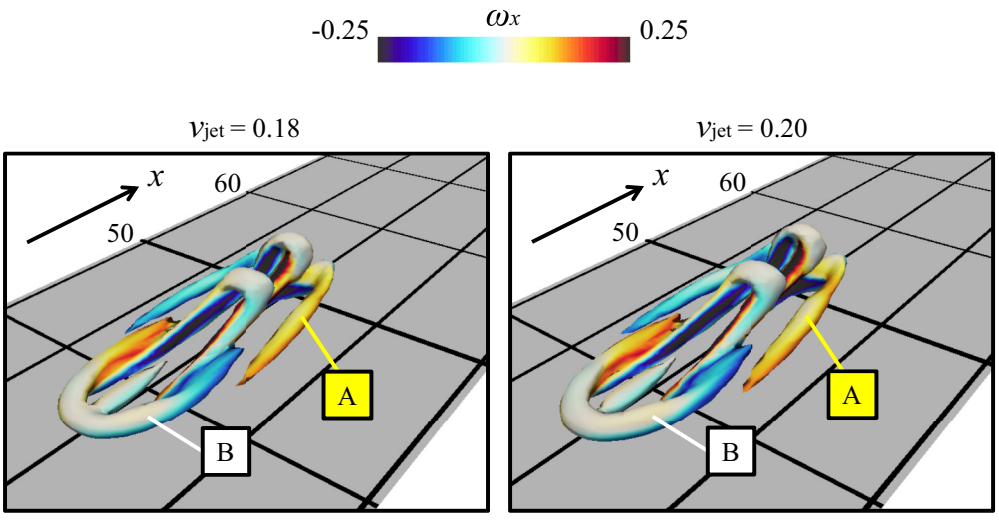

(a) $t = 34.6$

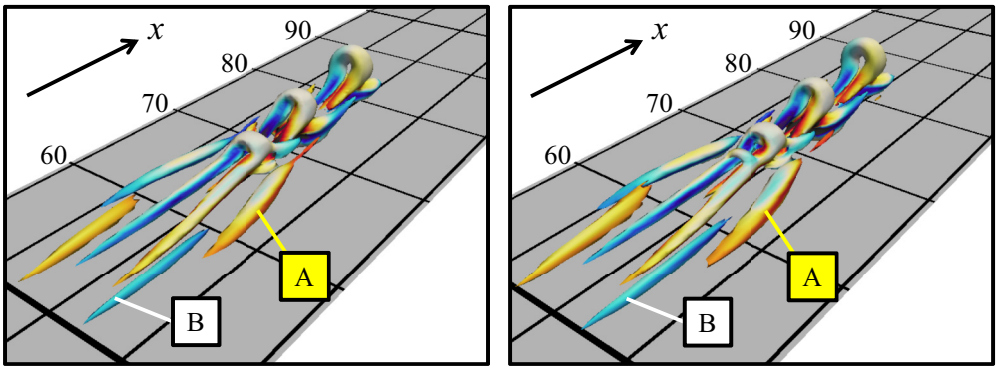

(b) $t = 69.1$

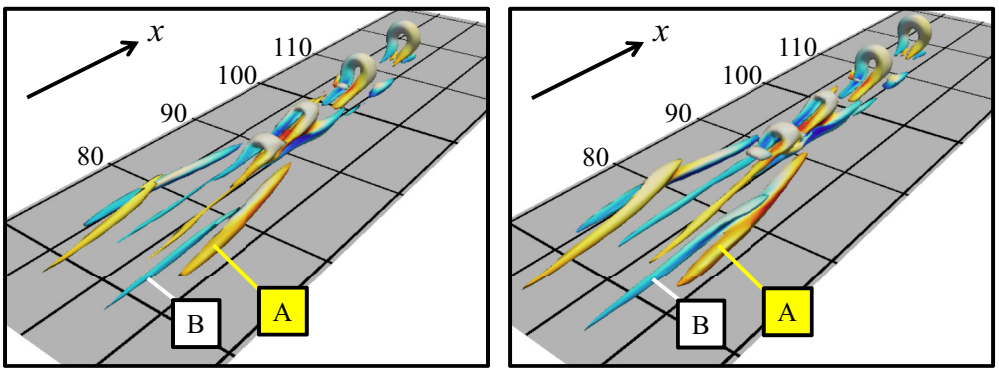

(c) $t = 103.7$

FIG. 4. (*Continued.*)

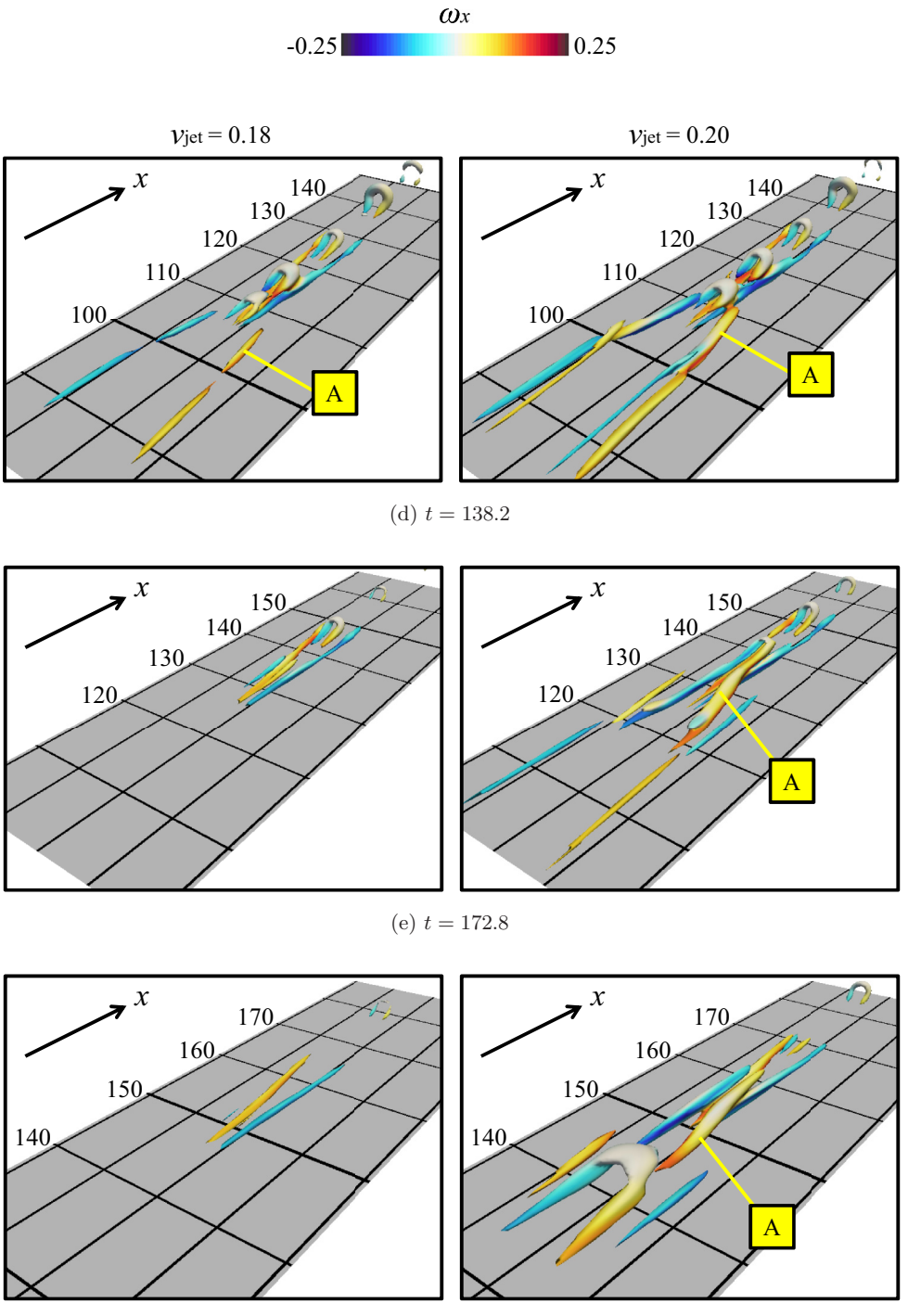

FIG. 4. Hairpin vortices of the first generation are shown by isosurfaces of $Q = 0.002$ for the $v_{\text{jet}} = 0.18$ and 0.20 cases, namely, the reference cases (A) and (B). The surfaces are colored depending on the local streamwise vorticity ω_x. Maxima of Q are (a) 0.193 and 0.249, (b) 0.084 and 0.087, (c) 0.024 and 0.028, (d) 0.017 and 0.024, (e) 0.008 and 0.012, and (f) 0.004 and 0.013, for the $v_{\text{jet}} = 0.18$ and 0.20 cases, respectively.

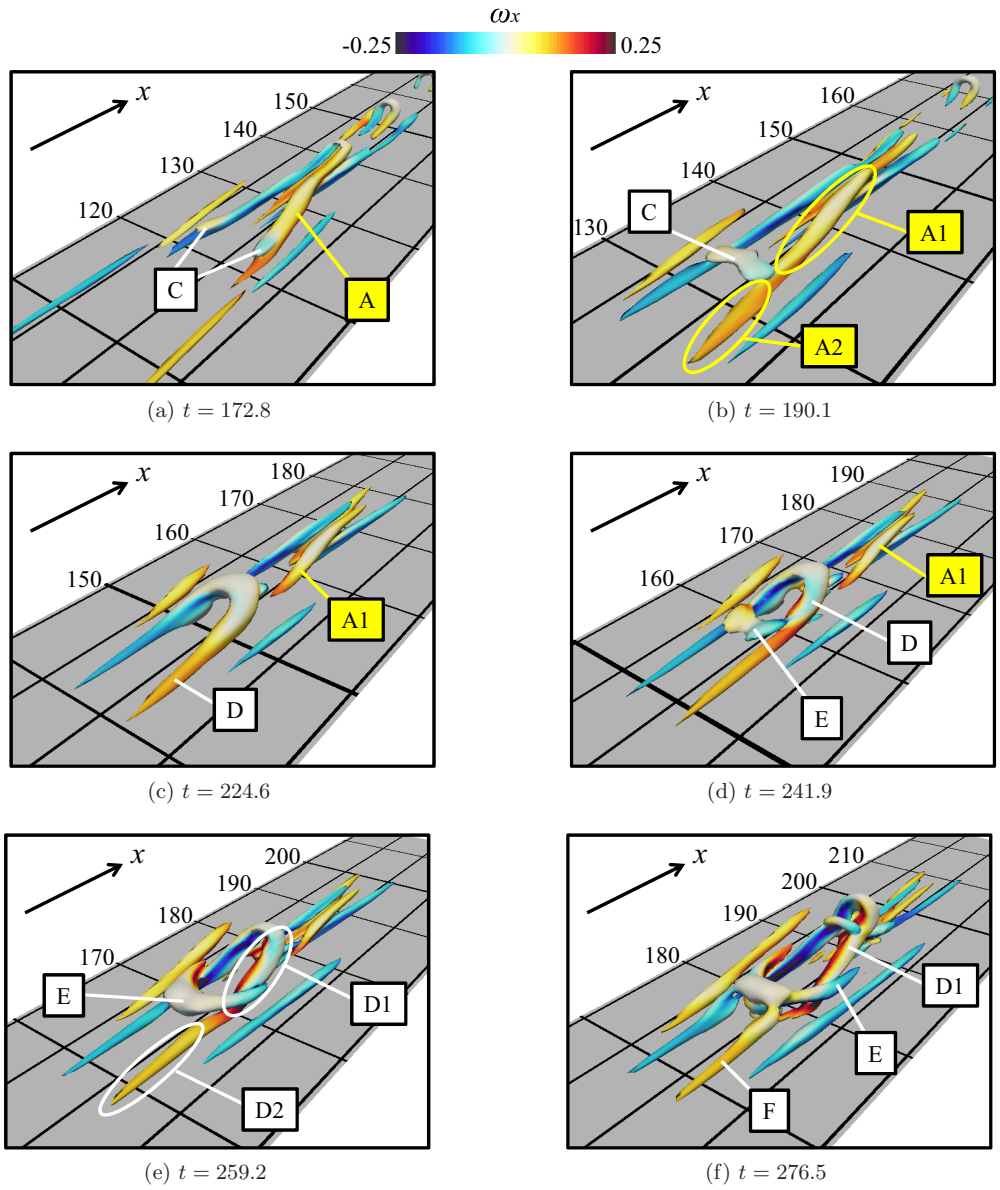

(a) $t = 172.8$ (b) $t = 190.1$

(c) $t = 224.6$ (d) $t = 241.9$

(e) $t = 259.2$ (f) $t = 276.5$

FIG. 5. (*Continued.*)

only the vortices within $|z| \leqslant 2$ are shown. The first-generation hairpin's distinctive characteristics are the head, which is raised nearly perpendicular to the wall, and the legs, which are close to each other in the z direction. Figure 7 shows the top and side views of the second-generation hairpin vortex D at $t = 224.6$. Only $|z| \leqslant 2.5$ is shown in the side view (b). Unlike the first generation, the spacing between the legs is wide, and its head is inclined in the positive x direction.

Next, the averaged streamwise vorticity $\overline{\omega_x}$, defined as

$$\overline{\omega_x} \equiv \frac{\iiint_K \omega_x dx\, dy\, dz}{\iiint_K dx\, dy\, dz}, \tag{1}$$

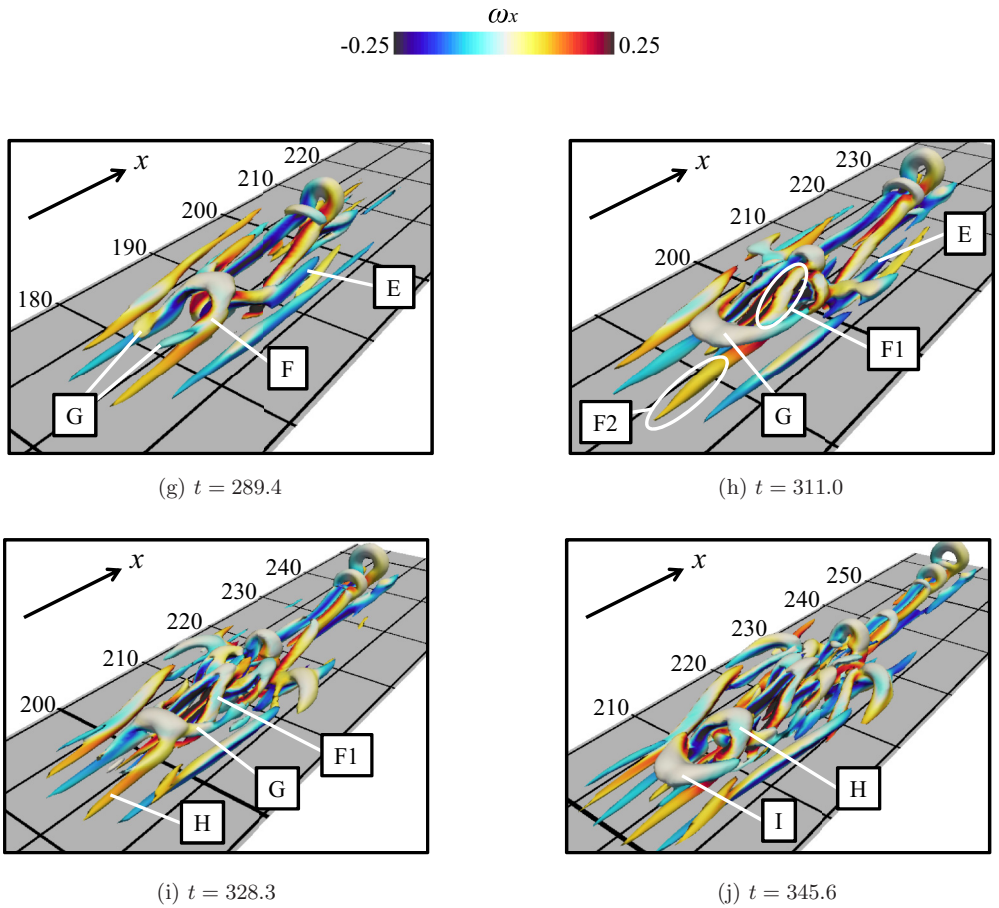

(g) $t = 289.4$ (h) $t = 311.0$

(i) $t = 328.3$ (j) $t = 345.6$

FIG. 5. Hairpin vortices of the second-generation are shown by isosurfaces of $Q = 0.002$ for the $v_{\text{jet}} = 0.20$ case [reference case (B)]. The surfaces are colored depending on the local streamwise vorticity ω_x. Maxima of Q are (a) 0.012, (b) 0.010, (c) 0.016, (d) 0.037, (e) 0.070, (f) 0.092, (g) 0.104, (h) 0.113, (i) 0.166, and (j) 0.180.

is calculated and compared between the first- and second-generation hairpin vortices. Here the region of integration, K, is where conditions $Q \geqslant 0.002$ and $z \geqslant 0$ are satisfied, while the head part of the hairpin vortex is excluded. As examples, the K regions are shown as red boxes in Fig. 6(a) and Fig. 7(a). The time variations of averaged streamwise vorticities $\overline{\omega_x}$ are presented in Fig. 8. The vorticities at the legs of the first-generation hairpins nos. 1 to 5 decrease with time, regardless of their initial values or when the hairpins are born. On the contrary, the averaged streamwise vorticity of second-generation hairpin D increases, even though its initial value is small. The locations of both ends of legs of the first-generation hairpins (nos. 1–5) and that of the second-generation hairpin D are obtained from Fig. 6(b) and Fig. 7(b), respectively. The differences between the local velocities at the two ends of the vortices can be measured. This value is found to be 0.238 for the second-generation hairpin D, and 0.049, 0.101, 0.238, 0.104, and 0.257 for the first-generation hairpins no. 1, 2, 3, 4, and 5, respectively. This result shows that the stretching speed of the second-generation hairpin D's leg is not considerably different from some of the first-generation hairpin legs. Therefore, the reason why the vorticity in the legs of the second-generation hairpin D increased while the vorticity in the legs of the first-generation hairpins did not increase cannot be solely attributed to the leg stretching. Another noteworthy point is the spacing between the hairpins' legs. As shown in Fig. 6(a), at $t = 103.7$, the legs of the first-generation hairpins 2 to 4 are found at $z = \pm 0.5$. On the other hand, as shown in

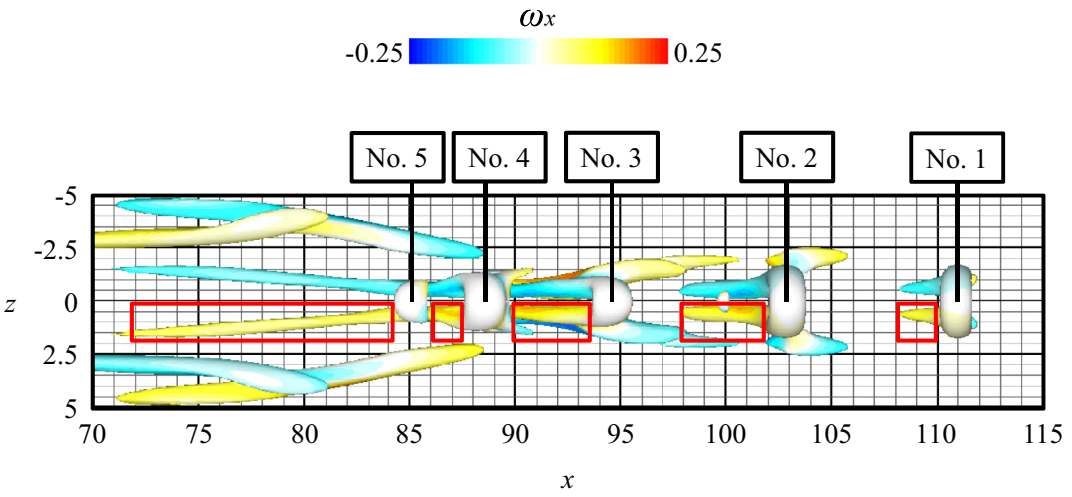

(a) Top view

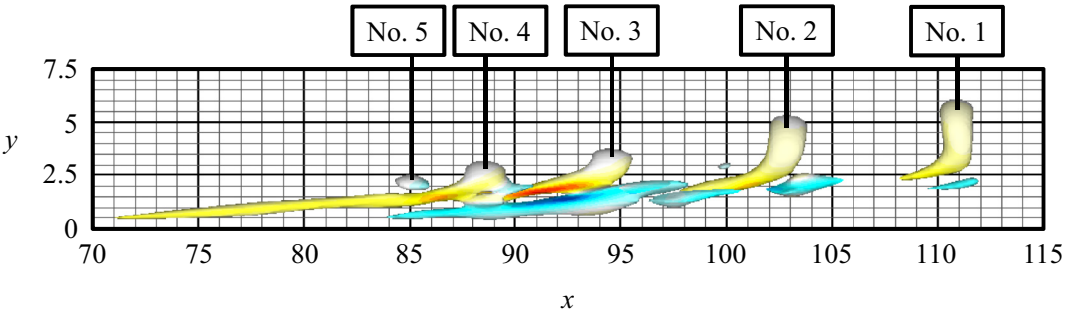

(b) Side view

FIG. 6. Top and side views of the hairpin vortices of the first generation visualized by $Q = 0.002$ at $t = 103.7$ for the $v_{\text{jet}} = 0.20$ case [reference case (B)]. The surfaces are colored depending on the local streamwise vorticity ω_x. Maximum of Q is 0.028.

Fig. 7(a), at $t = 224.6$, the legs of second-generation hairpin D are at $z = \pm 2$. Obviously, the spacings between the legs of the second-generation hairpins are much wider than those of the first-generation hairpins. Because the signs of the x-direction vorticities inside the two legs of a hairpin vortex are opposite, vorticities cancel each other with time owing to viscous diffusion. In the cases of the first-generation hairpins with smaller distances between the legs, the canceling effect is relatively large, causing hairpin vortices to decay quickly, while this is not so for the second-generation hairpins. Figure 9 shows the top views around the second-generation hairpins at $t = 289.4$ and 328.3. The distance between the legs at birth is large; however, the legs eventually get close together aligned in the streamwise direction similar to the first-generation hairpins. Under this configuration, their averaged streamwise vorticities decrease. The important point is that generations of many new vortical structures take place before second-generation hairpin D starts to decay.

C. Detailed generation mechanism of the second-generation hairpin vortex

It has been shown that the appearance of the second-generation hairpin vortex is the key to the generation of more complicated vortical structures leading to the turbulent transition. So, next, the generation process of the second-generation hairpin vortices is investigated in detail, focusing

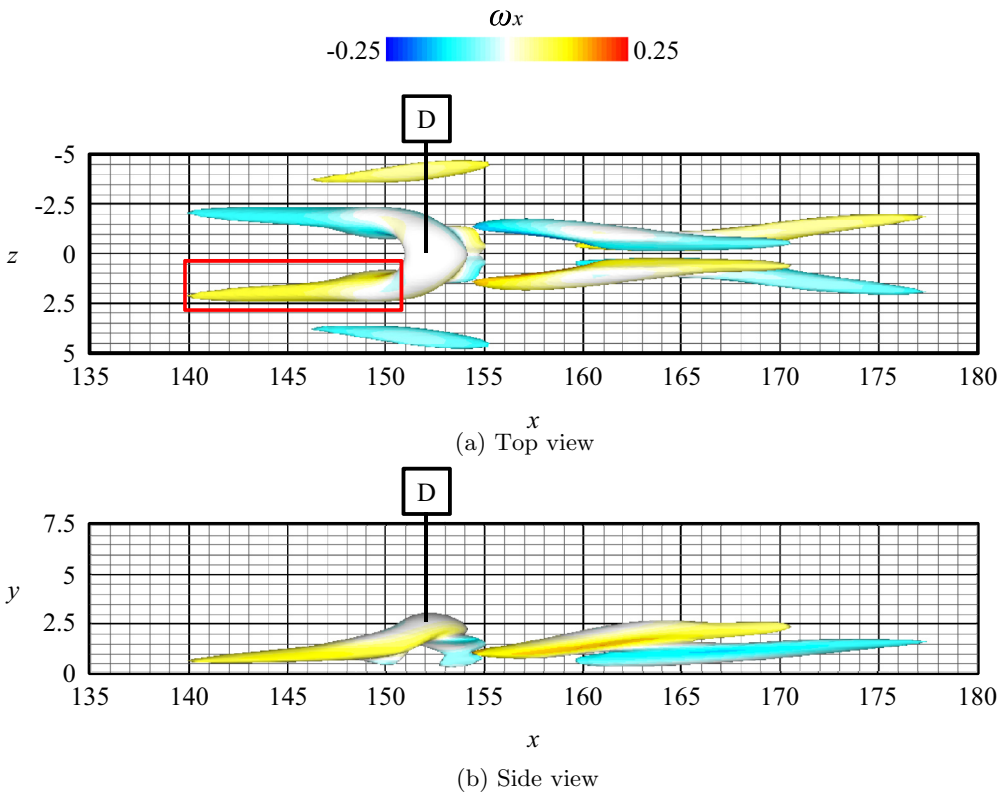

FIG. 7. Top and side views of the hairpin vortices of the second generation visualized by $Q = 0.002$ at $t = 224.6$ for the $v_{\text{jet}} = 0.20$ case [reference case (B)]. The surfaces are colored depending on the local streamwise vorticity ω_x. Maximum of Q is 0.016.

especially on the difference between the vortical structures observed in the two cases with two different jet velocities, $v_{\text{jet}} = 0.18$ [reference case (A)] and 0.20 [reference case (B)]. Figure 10 shows the top and side views of vortical structures from $t = 77.8$ through $t = 155.5$ for both jet conditions. At $t = 77.8$ in both jet-velocity cases, the downstream ends of the longitudinal vortex pair A marked by black ellipses in the figure are found at $|z| = 2$–3 on the sides of a first-generation hairpin. However, the difference can be observed at $t = 103.7$: in the stronger-jet case [reference case (B)], the tips of longitudinal-vortex pair A move slightly inward, closer to the hairpin vortex. In the weaker-jet case [reference case (A)] longitudinal vortices A gradually decay after $t = 138.2$. On the other hand, in the stronger-jet case [reference case (B)], longitudinal vortices A become connected to central hairpin vortex No. 5 and turn into its legs at $t = 155.5$. The newly formed hairpin vortex is the second-generation hairpin with a wide space between its legs. It should be noted that the legs of the second-generation hairpin are inclined as indicated by the red ellipse in Fig. 10(e), which will be strongly stretched by the velocity difference between the two ends of the leg.

Let us briefly look into the reason why the tips of longitudinal-vortex pair A moved inward. As shown in Fig. 11, the absolute value of the streamwise vorticity $\overline{\omega_x}$ of longitudinal vortex A, which is defined in the same way as in Eq. (1), is higher for the case of $v_{\text{jet}} = 0.20$ [reference case (B)]. Therefore, in the $v_{\text{jet}} = 0.20$ case [reference case (B)], the images will drive the vortices more inward, compared to the $v_{\text{jet}} = 0.18$ case [reference case (A)]. Under the flow conditions given in this research, the key to the boundary layer transition was whether or not the second-generation hairpins with widespread legs could be formed as a result of connections between the head of the first-generation hairpin and longitudinal vortices nearby. Once the first

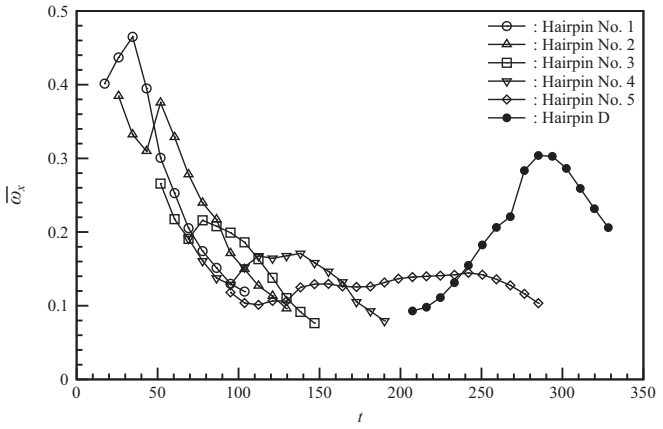

FIG. 8. Time variation of the averaged streamwise vorticity $\overline{\omega_x}$ of the legs of hairpin vortices of the first and second generations.

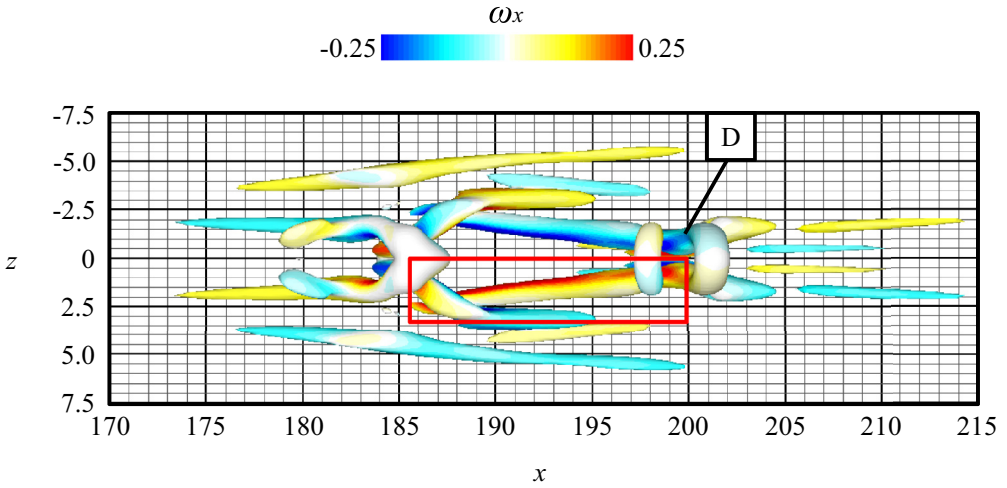

(a) $t = 289.4$

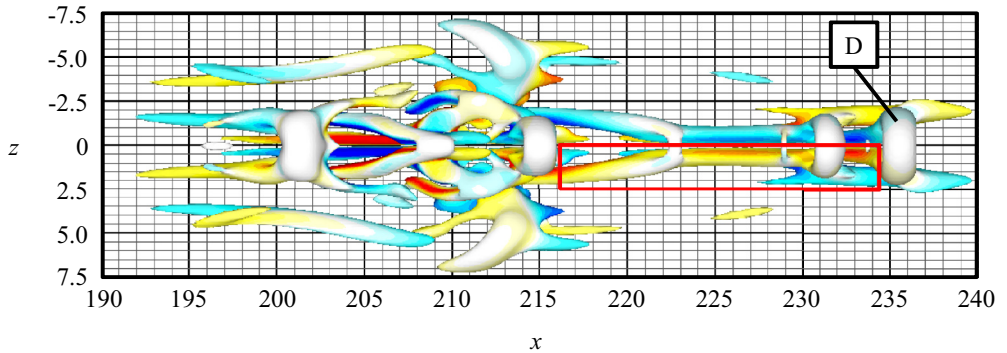

(b) $t = 328.3$

FIG. 9. Top views of the hairpin vortices of the second-generation visualized by $Q = 0.002$ for the $v_{\text{jet}} = 0.20$ case [reference case (B)]. The surfaces are colored depending on the local streamwise vorticity ω_x. Maxima of Q are 0.104 at (a) $t = 289.4$ and 0.166 at (b) $t = 328.3$.

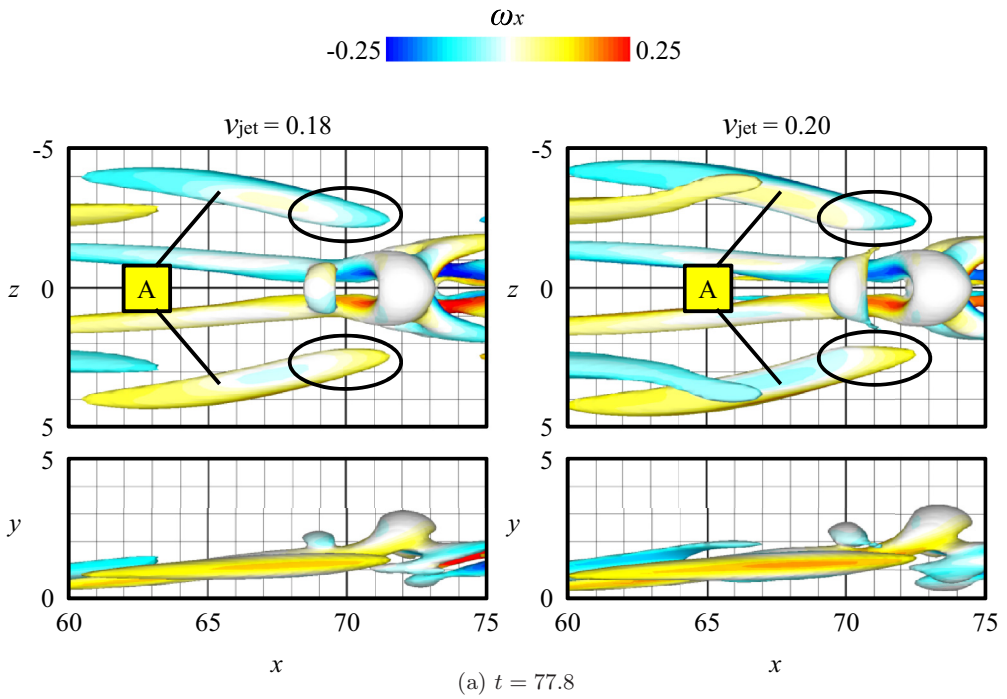

(a) $t = 77.8$

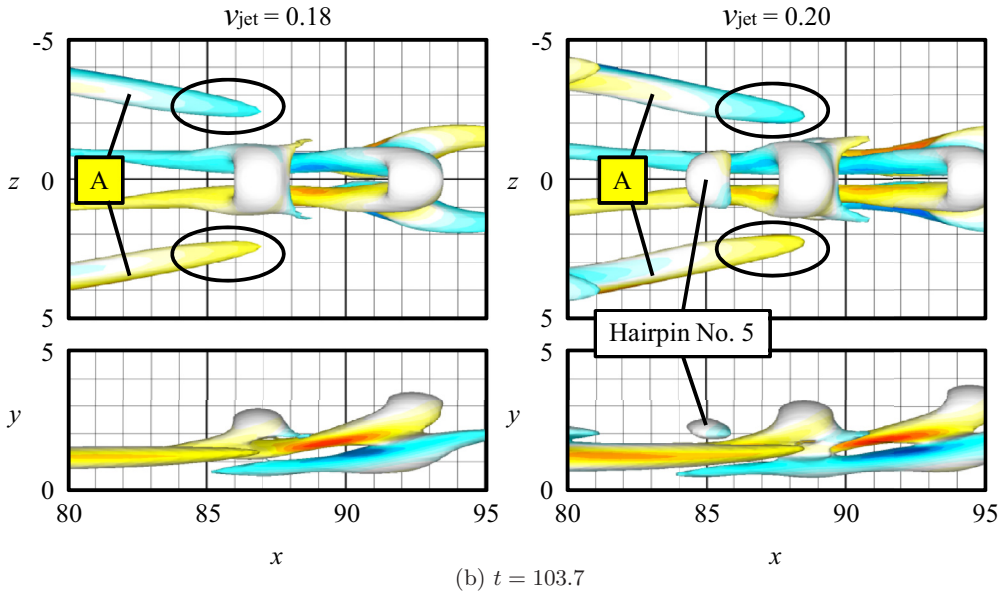

(b) $t = 103.7$

FIG. 10. (*Continued.*)

second-generation hairpin vortex was created, the new vortical structures appeared one after another. It is obvious that the second-generation hairpin vortex is the flow structure that can start the laminar-turbulent transition.

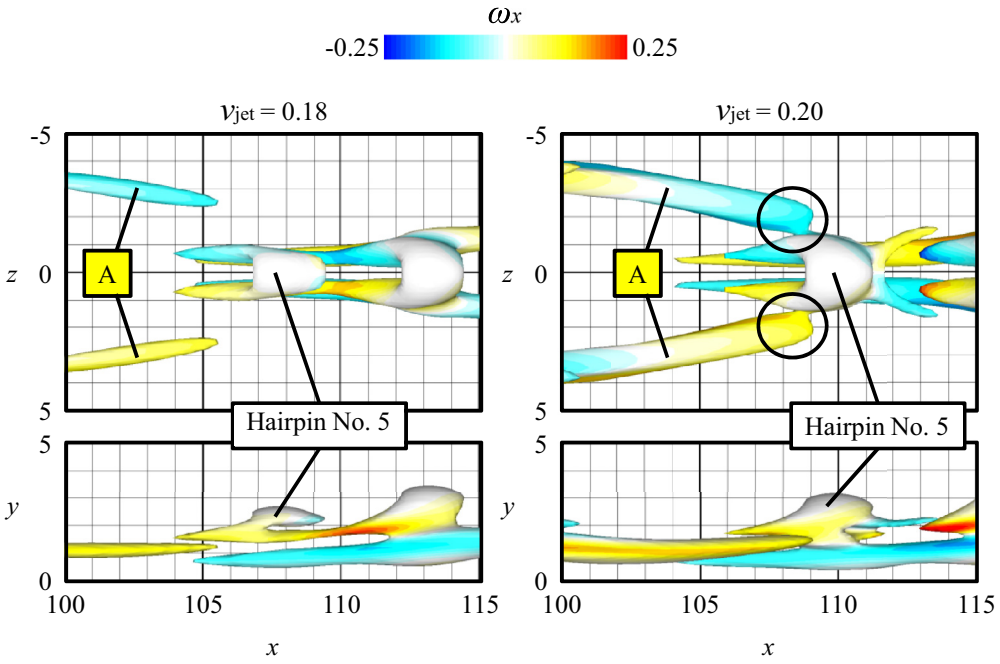

(c) $t = 138.2$

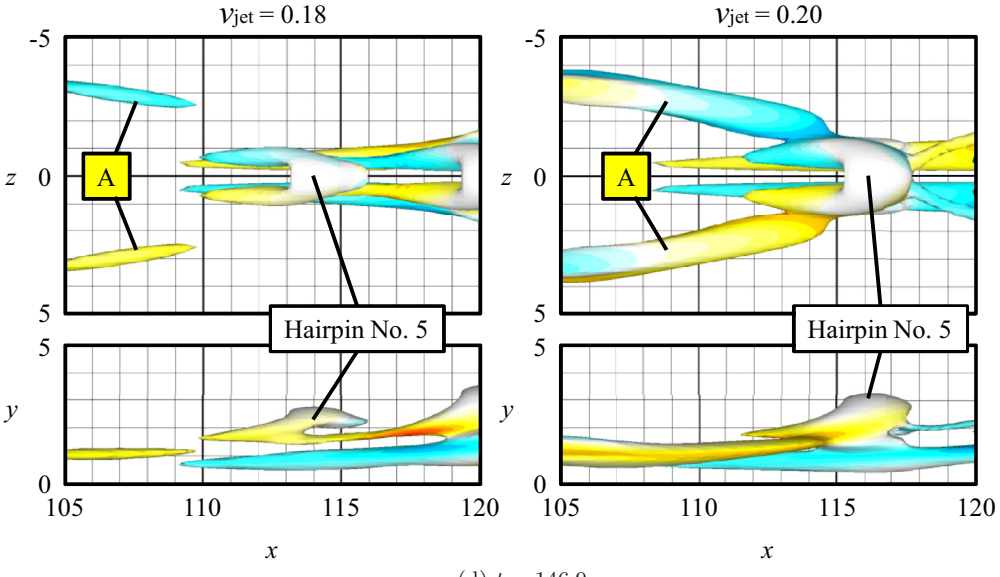

(d) $t = 146.9$

FIG. 10. (*Continued.*)

D. Turbulent transition under different jet-ejecting conditions

Simulations are performed under conditions different from that of the reference cases. These conditions are shown in Table I. The top two in Table I are the reference cases.

First, the jet location is changed to find the effect of the Reynolds number. It is found that the location of the jet does not considerably affect the vortical structures such as the first-generation

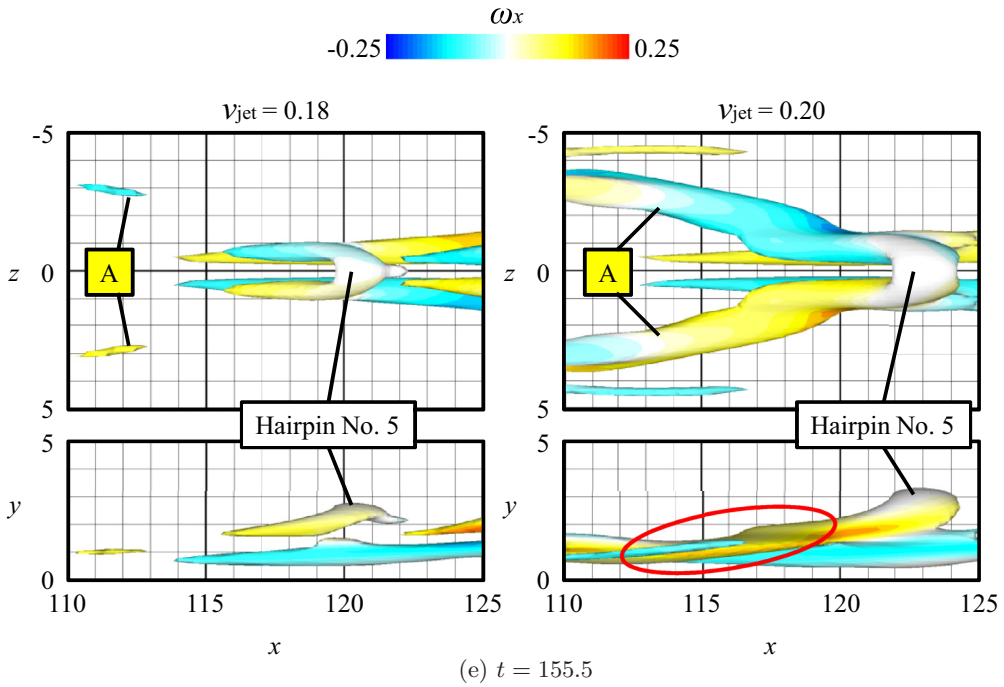

(e) $t = 155.5$

FIG. 10. Comparison of vortical structures around hairpin no. 5 visualized by $Q = 0.002$ for the $v_{\text{jet}} = 0.18$ and 0.20 cases [reference cases (A) and (B)]. The surfaces are colored depending on the local streamwise vorticity ω_x. Maxima of Q are (a) 0.060 and 0.061, (b) 0.024 and 0.028, (c) 0.017 and 0.024, (d) 0.016 and 0.021, and (e) 0.013 and 0.016, for the $v_{\text{jet}} = 0.18$ and 0.20 cases, respectively.

hairpins and the second-generation hairpins, although the critical jet velocity differed from case to case. Additionally, it is also found that whether the jet location is placed in the subcritical region ($\text{Re}_{\delta^*} = 456$) or in the supercritical region ($\text{Re}_{\delta^*} = 867$) does not make much of a difference to the vortical structures.

Second, the effect of the spanwise width of the jet region is checked. When the jet width is narrowed from 1.73 (reference) to 1.04, no difference is found in the results except that the spacings between the legs of the hairpins are narrower. Figure 12 shows the snapshots of vortical structures at $t = 103.7$, $t = 233.3$, and $t = 311.0$ when the spanwise width of the jet region is increased from 1.73 (reference) to 2.76. Further, the weaker-jet case of $v_{\text{jet}} = 0.16$ and the stronger-jet case of $v_{\text{jet}} = 0.18$

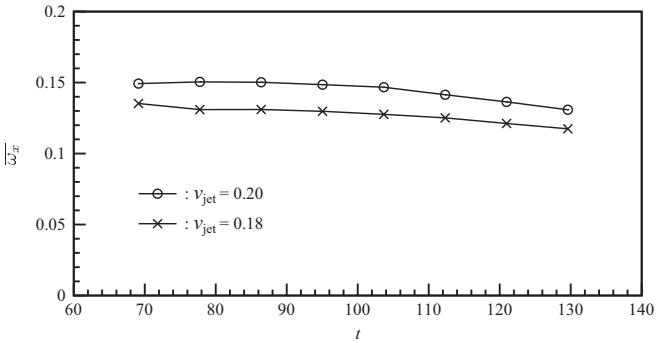

FIG. 11. Time variation of averaged streamwise vorticity $\overline{\omega_x}$, of the longitudinal vortices A.

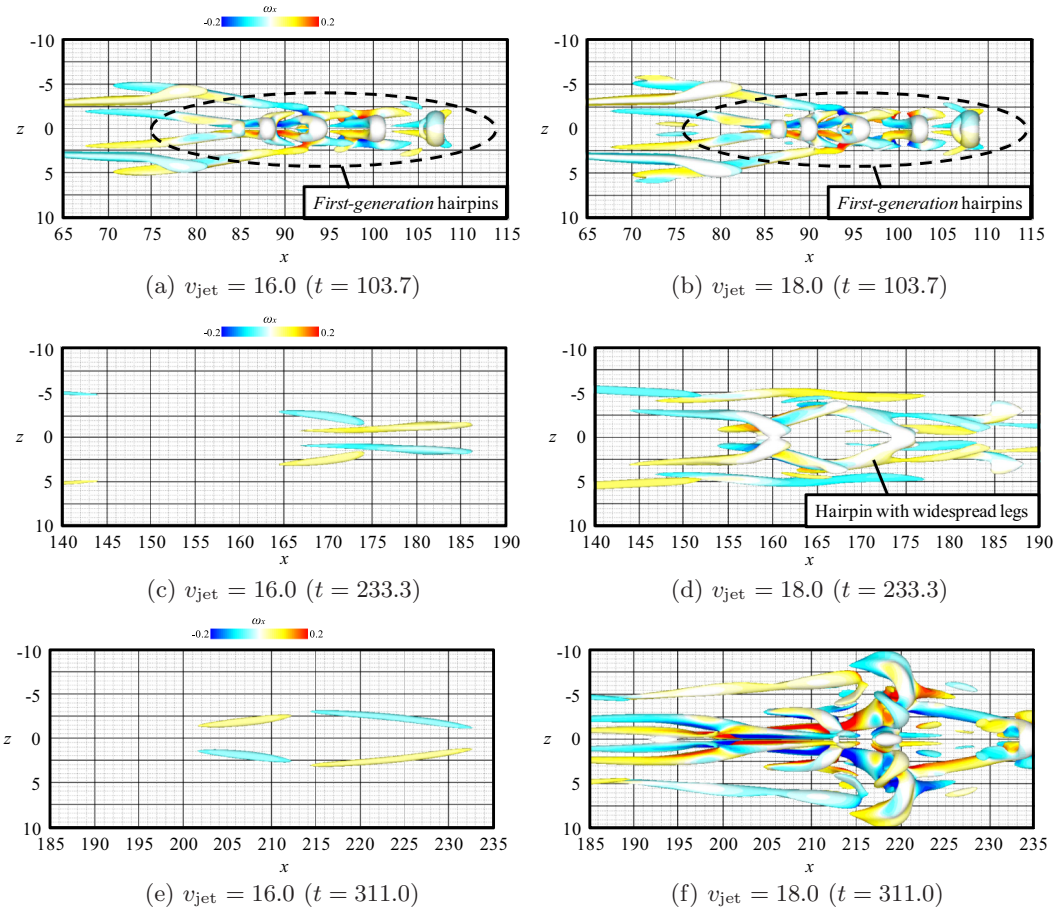

(a) $v_{\mathrm{jet}} = 16.0$ $(t = 103.7)$ (b) $v_{\mathrm{jet}} = 18.0$ $(t = 103.7)$

(c) $v_{\mathrm{jet}} = 16.0$ $(t = 233.3)$ (d) $v_{\mathrm{jet}} = 18.0$ $(t = 233.3)$

(e) $v_{\mathrm{jet}} = 16.0$ $(t = 311.0)$ (f) $v_{\mathrm{jet}} = 18.0$ $(t = 311.0)$

FIG. 12. Top views of the vortical structures visualized by $Q = 0.001$ for the cases with jet ejection from a wide hole. The surfaces are colored depending on the local streamwise vorticity ω_x. Maxima of Q are (a) 0.046, (b) 0.036, (c) 0.003, (d) 0.029, (e) 0.002, and (f) 0.127.

are compared. Note that in this section, isosurfaces of $Q = 0.001$ are used for the identification of vortical structures. At $t = 103.7$, similar first-generation hairpin vortices can be found in both cases. At $t = 233.3$, as shown in Figs. 12(c) and 12(d), a second-generation hairpin can be found in each of the two figures, although their strengths are different. In the weaker-jet case of $v_{\mathrm{jet}} = 0.16$, the hairpin is apparently very weak with its head missing, while in the stronger $v_{\mathrm{jet}} = 0.18$ jet case, the second-generation hairpin appears more robust and is surrounded by many other vortices. Later at $t = 311.0$, shown in Figs. 12(e) and 12(f), the difference between the weaker and stronger-jet cases becomes more obvious. Although the structure of vortices found in Fig. 12(f) appears to be different from the reference case (B) (Fig. 5), there is no difference in the basic sequence, which is that the first-generation hairpins are followed by the second-generation hairpin followed by the complicated vortical structures.

Finally, the influence of the duration of jet ejection is investigated. The ejection duration T_{jet} is increased from 13.0 up to 19.0, while keeping the jet velocity v_{jet} the same at 0.18. Although the flow field returns back to the laminar state when the ejection duration T_{jet} is 13.0 [reference case (A)], the turbulent transition occurs when $T_{\mathrm{jet}} = 19.0$. Figure 13 shows snapshots of the vortical structures at $t = 103.7$, $t = 172.8$, and $t = 311.0$. As shown in Figs. 13(a) and 13(b), at $t = 103.7$ the first-generation hairpin vortices in both cases are not considerably different. At $t = 172.8$, the

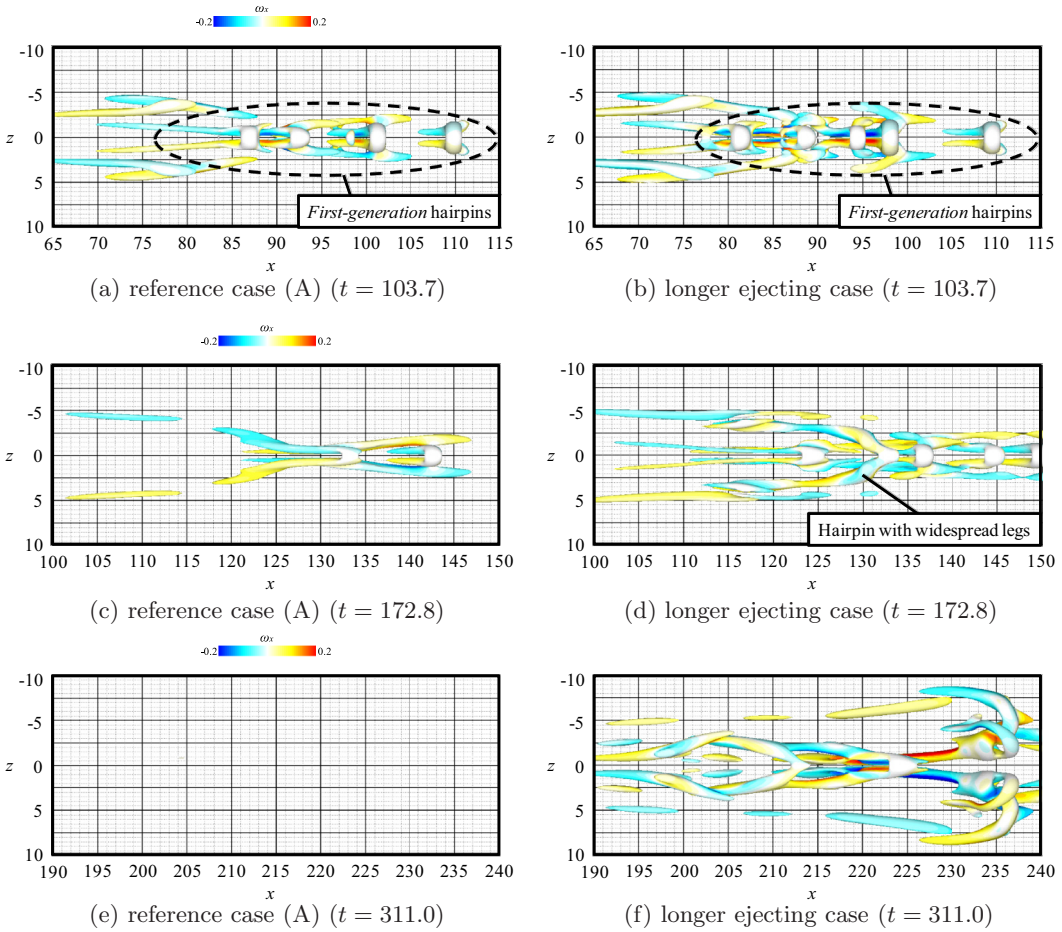

(a) reference case (A) ($t = 103.7$) (b) longer ejecting case ($t = 103.7$)

(c) reference case (A) ($t = 172.8$) (d) longer ejecting case ($t = 172.8$)

(e) reference case (A) ($t = 311.0$) (f) longer ejecting case ($t = 311.0$)

FIG. 13. Top views of the vortical structures visualized by $Q = 0.001$ for the $v_{\text{jet}} = 0.18$ cases when the duration of the jet T_{jet} is changed. The surfaces are colored depending on the local streamwise vorticity ω_x. Maxima of Q are (a) 0.024, (b) 0.045, (c) 0.008, (d) 0.023, (e) 0.001, and (f) 0.078.

second-generation hairpins appear only in the longer ejecting case [Fig. 13(d)]. A trace of the similar structure can be found in $x = 120$–125 of Fig. 13(c); however, the vortical structure is much weaker. At $t = 311.0$ shown in Figs. 13(e) and 13(f), there are no vortical structures in the $T_{\text{jet}} = 13.0$ case [reference case (A)], whereas complicated vortical structures appear in the $T_{\text{jet}} = 19.0$ case. The complicated structures of the vortices found in Fig. 13(f) are not the same as the reference case (B) (Fig. 5), nor that of Fig. 12(f). This result indicates that the turbulent transition can be triggered using an even weaker jet if the jet ejection duration is sufficiently long and that the path to turbulence is basically not different from the reference case (B).

In all the cases studied here, the basic sequence of the appearance of the first-generation hairpins followed by the second-generation hairpin with widespread legs and finally the generation of complicated vortical structures, was the same. Although the complicated vortical structures created downstream were different between the studied cases, the second-generation hairpin with widespread legs played a key role in all cases.

IV. CONCLUSIONS

In this numerical study, short-duration jets with different velocities were ejected into a Blasius boundary layer in order to find a vortical structure serving as the key to a laminar-turbulent transition.

When the jet velocity exceeded a certain threshold velocity, the laminar-turbulent boundary layer transition took place downstream, whereas, when the jet velocity fell below this value, the generated disturbances inside the boundary layer decayed, and the disturbed boundary layer went back to the laminar state. Thus, the reason for the large difference between the two cases was investigated in detail. The ejection duration, the aspect ratio of ejection hole, and the ejection location were also changed and the results were compared.

In both cases of strong and weak jets, the first-generation hairpin vortices were generated, which did not directly lead to transition. Only in the stronger-jet case, a second-generation hairpin vortex with widespread legs was generated. Once the second-generation hairpin vortex appeared in the boundary layer, new vortical structures were generated one after another, leading to a laminar-turbulent boundary layer transition. The creation process of the second-generation vortices was studied in detail by tracking the vortex deformation and interaction. It was found that the second-generation hairpin was created through the connection of the head of the most upstream first-generation hairpin to a pair of nearby longitudinal vortices, which became the new legs of the hairpin. The second-generation hairpin would become stronger because its legs would be stretched by the velocity gradient of the boundary layer, and this vortex triggered the sequence of generations of vortical structures.

In our studies of different jet-ejecting conditions, we found that a weaker jet could trigger the boundary layer transition if the jet was ejected for a longer period. Changing the streamwise location, the spanwise width of the jet hole, or the jet-ejecting duration did not affect the basic sequence of the appearance of the first-generation hairpins followed by the second-generation hairpin with widespread legs and finally the generation of complicated vortical structures.

These results show that the onset of turbulence could be attributed to a small difference in the arrangement and strengths of vortical structures in a boundary layer, which determined whether the hairpin vortices with widespread legs were generated. Although we could identify a single structure which serves as the key for the laminar-turbulent boundary layer transition under several flow conditions, it is difficult to believe that it is the only one for all the transition paths. We hope further investigations may lead to the finding of a key structure that is universally important in all boundary layer transitions.

ACKNOWLEDGMENT

Part of the computational results in this paper were obtained using supercomputing resources at the Cyberscience Center, Tohoku University.

[1] Y. S. Kachanov, Physical mechanisms of laminar-boundary-layer transition, Annu. Rev. Fluid Mech. **26**, 411 (1994).

[2] P. Schlatter, L. Brandt, H. C. de Lange, and D. S. Henningson, On streak breakdown in bypass transition, Phys. Fluids **20**, 101505 (2008).

[3] M. Asai, Y. Konishi, Y. Oizumi, and M. Nishioka, Growth and breakdown of low-speed streaks leading to wall turbulence, J. Fluid Mech. **586**, 371 (2007).

[4] M. Gaster, The development of three-dimensional wave packets in a boundary layer, J. Fluid Mech. **32**, 173 (1968).

[5] M. Gaster and I. Grant, An experimental investigation of the formation and development of a wave packet in a laminar boundary layer, Proc. R. Soc. Lond. A. **347**, 253 (1975).

[6] M. Asai and M. Nishioka, Boundary-layer transition triggered by hairpin eddies at subcritical Reynolds numbers, J. Fluid Mech. **297**, 101 (1995).

[7] G. Lemoult, J. Aider, and J. E. Wesfreid, Experimental scaling law for the subcritical transition to turbulence in plane Poiseuille flow, Phys. Rev. E **85**, 025303(R) (2012).

[8] O. Levin and D. S. Henningson, Turbulent spots in the asymptotic suction boundary layer, J. Fluid Mech. **584**, 397 (2007).
[9] B. A. Singer and R. D. Joslin, Metamorphosis of a hairpin vortex into a young turbulent spot, Phys. Fluids **6 (11)**, 3724 (1994).
[10] S. Cherubini, P. DePalma, J.-Ch. Robinet, and A. Bottaro, Rapid path to transition via nonlinear localized optimal perturbations in a boundary layer flow, Phys. Rev. E **82**, 066302 (2010).
[11] S. Cherubini, P. DePalma, J.-Ch. Robinet, and A. Bottaro, Edge states in a boundary layer, Phys. Fluids **23**, 051705 (2011).
[12] B. A. Singer, Characteristics of a young turbulent spot, Phys. Fluids **8 (2)**, 509 (1996).
[13] M. Farano, S. Cherubini, J.-Ch. Robinet, and P. DePalma, Hairpin-like optimal perturbations in plane Poiseuille flow, J. Fluid Mech. **775**, R2 (2015).
[14] M. S. Acarlar and C. R. Smith, A study of hairpin vortices in a laminar boundary layer. Part 2. Hairpin vortices generated by fluid injection, J. Fluid Mech. **175**, 43 (1987).
[15] M. Skote, J. H. Haritonidis, and D. S. Henningson, Varicose instabilities in turbulent boundary layers, Phys. Fluids **14 (7)**, 2309 (2002).
[16] J. Philip and J. Cohen, Formation and decay of coherent structures in pipe flow, J. Fluid Mech. **655**, 258 (2010).
[17] V. Mehta and J. Cohen, Experimental investigation of a low-amplitude transition in pipe flow, Fluid Dyn. Res. **48**, 061428 (2016).
[18] J. Zhou, R. J. Adrian, S. Balachandar, and T. M. Kendall, Mechanisms for generating coherent packets of hairpin vortices in channel flow, J. Fluid Mech. **387**, 353 (1999).
[19] S. Bagheri, P. Schlatter, P. J. Schmid, and D. S. Henningson, Global stability of a jet in crossflow, J. Fluid Mech. **624**, 33 (2009).
[20] K. Mahesh, The interaction of jets with crossflow, Annu. Rev. Fluid Mech. **45**, 379 (2013).
[21] A. R. Karagozian, The jet in crossflow, Phys. Fluids **26**, 101303 (2014).
[22] T. Kawamura, H. Takami, and K. Kuwahara, Computation of high Reynolds number flow around a circular cylinder with surface roughness, Fluid Dyn. Res. **1**, 145 (1986).
[23] K. Kuwahara and S. Komurasaki, Simulation of high Reynolds number flows using multidirectional upwind scheme, AIAA Paper 2002-0133 (2002).
[24] J. Peixinho and T. Mullin, Finite-amplitude thresholds for transition in pipe flow, J. Fluid Mech. **582**, 169 (2007).
[25] D. R. Sabatino and T. Rossmann, Tomographic PIV measurements of a regenerating hairpin vortex, Exp. Fluids **57**, 6 (2016).